Shear Shock Waves Observed in the Brain

David Espíndola,* Stephen Lee, and Gianmarco Pinton†

Joint Department of Biomedical Engineering, University of North Carolina at Chapel Hill, 109 Mason Farm Road, CB 7575, Chapel Hill, North Carolina 27514, USA and North Carolina State University, 4130 Engineering Building III, CB 7115, Raleigh, North Carolina 27695, USA

(Received 13 December 2016; revised manuscript received 12 June 2017; published 31 October 2017)

The internal deformation of the brain is far more complex than the rigid motion of the skull. An ultrasound imaging technique that we have developed has a combination of penetration, frame-rate, and motion-detection accuracy required to directly observe the formation and evolution of shear shock waves in the brain. Experiments at low impacts on the traumatic-brain-injury scale demonstrate that they are spontaneously generated and propagate within the porcine brain. Compared to the initially smooth impact, the acceleration at the shock front is amplified up to a factor of 8.5. This highly localized increase in acceleration suggests that shear shock waves are a previously unappreciated mechanism that could play a significant role in traumatic brain injury.

DOI: 10.1103/PhysRevApplied.8.044024

I. INTRODUCTION

Traumatic brain injuries (TBIs) are a major source of death and disability worldwide. Falls and motor-vehicle-related accidents are the largest contributors. Current biomechanical predictive criteria for TBI are based on measurements of skull motion such as linear and rotational acceleration [1,2]. Although the relationship between skull motion and injury has been extensively tested [2–7], mechanisms relating the two have not been conclusively established [8] due to the complexity of the deformation of the brain [9–11], which behaves as a nonlinear viscoelastic medium. *In situ* measurements of the rapid transient motion of the whole brain during a traumatic event may establish a more accurate biomechanical description of injury.

Shear vibration experiments on small brain samples have shown that the stress-strain relationship behaves nonlinearly for amplitudes as low as 1% [12,13], which is well below the strain threshold for injury [7,14,15]. Therefore, even mild injuries typically occur within the nonlinear elastic regime. Furthermore, the brain's shear wave speed ($c_t \sim 2$ m/s) is 3 orders of magnitude smaller than the compressional wave speed ($c_p \sim 1500$ m/s); therefore, the deformation from an impact is almost entirely in shear mode.

Aside from ultrasound, current methods that measure brain motion cannot capture this nonlinear behavior of shear waves due to limitations in frame rate, penetration, or motion-detection accuracy. For instance, magnetic resonance elastography (MRE) has been used to investigate shear wave propagation in the brain, typically at frame rates on the order of tens of images per second. Furthermore, the temporal sampling of MRE is fundamentally limited to a few milliseconds by the finite integration time over the spin relaxation [16,17]. The harmonics generated by nonlinear shear wave propagation exceed these sampling capabilities. Optical methods have larger frame rates, and they can measure motion in optically transparent materials [18–20]. However, they are limited to shallow penetration depths in soft tissue (approximately 2 mm) [21].

The only experimental corroboration of nonlinear shear waves and its characteristic harmonic signature was made over a decade ago in a homogeneous gelatin phantom [22]. These experimental methods were derived from ultrasound elastography [23] and performed with a high-frame-rate (3000 images/s) ultrasound scanner and a cross-correlation tracking algorithm that measured the interframe displacement. The high imaging rate was required to capture the rapid, transient, and broadband nature of the shocks. At these high frame rates, the movement between successive acquisitions is small (about 1 μm) and a highly accurate motion measurement is required. Although these gelatin phantoms are calibrated to have the same linear elastic properties as soft tissue (Young's modulus) they do not mimic the nonlinear and attenuating properties of brain, which are key components needed to characterize the shock-wave physics.

Despite this experimental report of shear shock waves in a homogeneous gelatin, there have been no reports of shear shock waves in the human body, including the brain. This lack of experimental observations is due to the difficulty of observing nonlinear shear displacements at depth and at high frame rates in the brain which include (1) the more challenging imaging environment, arising from the heterogeneous acoustical properties of its biological structures, and (2) the higher attenuation of the shear waves. To measure the shear shock-wave propagation in *ex vivo*

*david.espindola@unc.edu
†gfp@unc.edu

porcine brain presented in this article, we address these two challenges. We design a focused high-frame-rate ultrasound imaging sequence that has better penetration and is more accurate compared to previous plane-wave methods, and it is described here. These data are then processed with an adaptive tracking algorithm that can accurately characterize the almost discontinuous velocity profile at the shock fronts (see Appendix C and Ref. [24]). With these advancements, motion is detected at high frame rates and with high accuracy for all points within an imaging field of view as deep as the brain. It is shown that shear shock waves are spontaneously generated in the brain, i.e., a smooth excitation at the brain surface develops into a shock as it propagates within the brain. We show that the strong gradients at the shock front dramatically increase the local acceleration, strain, and strain rate in soft tissue, which suggests that this is a primary injury mechanism for a broad range of TBIs.

II. EXPERIMENTAL SETUP

The experimental design used to generate and measure shear shock waves in the brain is illustrated in Fig. 1. Porcine brains (8-week-old Yorkshire cross pigs) are extracted 1 h postmortem to minimize tissue degradation and are embedded in gelatin. Graphite powder (10–100 μm) is added to the gelatin with a concentration of 1% to generate acoustical contrast for the ultrasound images. The shear wave speed of the gelatin is calibrated by setting the concentration of 225-bloom gelatin to 5.0 wt %. This concentration yields a shear wave speed equivalent to measurements performed in porcine brains (2.14 ± 0.06 m/s; see Appendix A). The speed of sound is calibrated by adding 5.0% isopropyl alcohol to obtain a speed of 1490 m/s [26]. Before the gelatin cured, a 6-mm-thick acrylic plate is embedded near the surface of the brain, as shown in Fig. 1. Then, the plate is connected to an electromechanical shaker, and the gel is allowed to cool and cure in an ice-water bath.

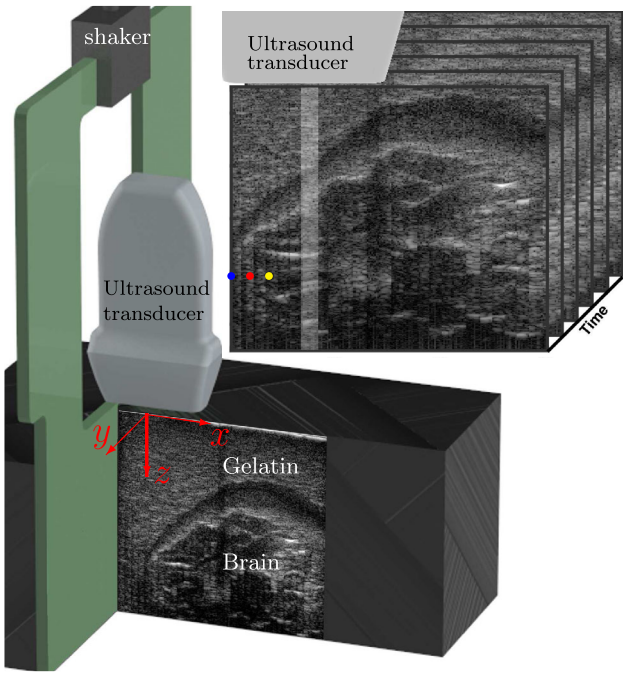

FIG. 1. A plate is embedded in gelatin brain to transmit shear waves with an electromechanical shaker. The shear wave produces displacement along depth (z), and it propagates along the x axis. The B-mode sequence is acquired from 32 synchronized, focused transmit-receive events. The focal depth is kept constant (60 mm) and each lateral focus position is shifted. The highlighted vertical stripe shows the region corresponding to a single transmit-receive event [25].

By matching the shear and compressional wave speeds between the brain and gelatin, a high transmission coefficient is obtained at the gelatin-brain interface. This is a nonbiofidelic interface since, *in vivo*, the impact energy has to be transmitted through layers of skull, meninges, cerebrospinal fluid, etc. The effect of the skull's shape is also ignored, although simulations indicated that the spherical nature of the skull facilitates the formation of shear shock waves deep in the brain by virtue of its natural focal geometry [27]. However, the complex boundary conditions at the skull-brain interface would generate wave fields that are currently not solvable by either theoretical or numerical methods in the nonlinear regime. Instead, narrow-band planar waves provide conditions for which theoretical results are known. Typically, impacts that cause injury would not generate a pure polarized shear wave. Furthermore, they have a short duration and a broad power spectrum. Here, we generate a 75-Hz wave train, which is within the range of frequencies measured during head impacts (10–300 Hz) [6,28] and allow several cycles to be supported within the porcine brain. It has 5 cycles and a −80-dB Chebyshev envelope. This spectrally narrow signal has good separability in the frequency domain, which is necessary for the observation of the harmonic development and its comparison to theoretical predictions of shear shock-wave development. Note that the physics of shock-wave steepening and formation remains applicable to other loading conditions, such as impulse loading. This pulse is sent to a power amplifier to generated amplitudes up to 450 m/s^2, as measured by a linear accelerometer attached to the plate. This setup generates linearly polarized shear plane waves with a full control of its frequency content. The shear wave induces a movement in the z axis and it is propagated through the x axis.

Shear wave propagation through the brain and gelatin is monitored with a research ultrasound scanner (Verasonics). A 5-MHz commercial diagnostic ultrasound imaging probe (ATL Philips L7-4) is positioned above the phantom, as shown in Fig. 1, using a high-precision (10-μm) robotic arm to monitor different sections of the brain.

Conventional planar and plane-wave compounding [29] are sensitive to off-axis clutter and do not perform

optimally for *ex vivo* brain tracking. Sources of ultrasound image degradation, such as reverberation [30] and bright off-axis targets, which generate static and dynamic artifacts, decrease the image quality and degrade motion-tracking performance. This difficulty motivates the development of an alternative sequence which consists of 16 transmit-receive events focused at different lateral positions, each one with an F number of 4 and a focal depth of 6 cm. Each transmit-receive event generates 1200 frames of raw acoustical data. Then, a delay-and-sum beam-forming algorithm generates, from every event, eight A lines of focused rf data (see the highlighted area in Fig. 1). To maintain a high frame rate, each transmit-receive event is synchronized to the shear wave generation. Furthermore, to increase the visualization field, the acoustical probe is mechanically displaced to a second position using the robotic arm (see Appendix B). Thus, the images shown in this article are generated from 32 synchronized transmit-receive sequences, with an effective frame rate of 6200 frames/s. The jitter error on the synchronization time is measured to be 380 ns, which is equivalent to a 1/35 000 of a period at 75 Hz. The experiment is performed on four different brains. For each brain, seven amplitudes are used, ranging between 122 and 449 m/s^2. Five independent realizations are obtained for each amplitude by translating the transducer along the y axis, yielding a total of 35 experiments for each brain. All of the experiments are performed within 15 h postmortem at a temperature of 1 °C.

The ultrasound data are used to generate a high-frame-rate B-mode movie that illustrates the brain anatomy and the movement induced by the shear deformation (Fig. 1) [25]. We determine brain motion based on the beamformed rf data with a motion-detection algorithm designed to track the large discontinuous velocities associated with shear shock waves [24]. These shear excitations result in interframe deformations that change the relative scatterer positions and reduce the correlation between frames. The tracking algorithm uses a quality weighted three-dimensional median filter to iteratively optimize the correlation values, and it is calibrated to preserve the high-frequency displacements necessary to characterize the sharp shock front (see Appendix C for validation using simulated ultrasound imaging [31,32] and Rusanov solutions of cubically nonlinear shocks).

III. RESULTS AND DISCUSSION

Three snapshots of the resulting high-frame-rate movie of particle velocity [25] are shown in Fig. 2(a) for the case where the amplitude of the particle velocity at the plate is $v_0 = 1$ m/s, which produces a Mach number of $M = c_T/v_0 = 0.49$. A quasiplanar wave propagating from left to right can be clearly observed. Owing to the high Mach number, the brain develops a nearly discontinuous velocity profile in Fig. 2(b).

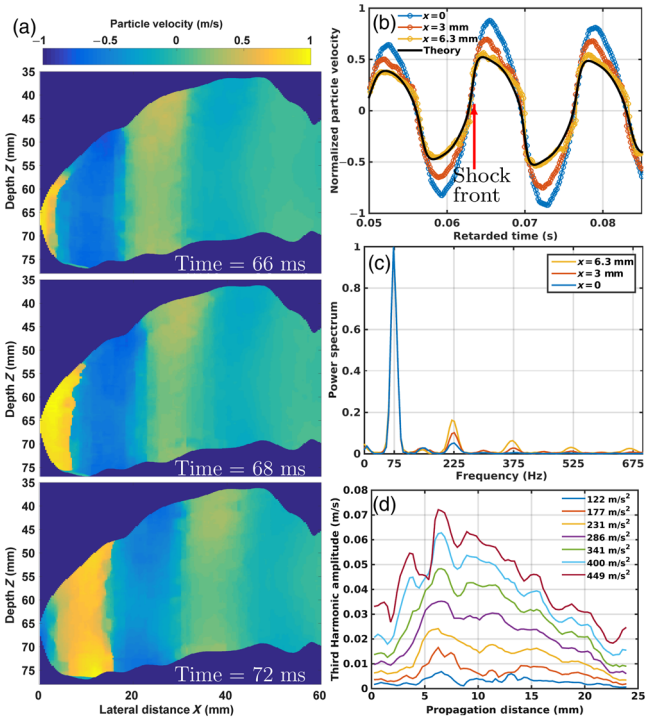

FIG. 2. (a) Snapshots of particle velocity generated by a planar shear wave propagating in the brain [25]. The initial condition is 449 m/s^2. (b) The evolution of shear wave propagation in the time domain shows excellent agreement with theoretical predictions for a homogeneous medium (the black line). (c) The specific odd-harmonic development is visible in the frequency domain. The curves in (b) and (c) correspond to the motion at single points represented by circles in Fig. 1. (d) As the driving amplitude increases, so does the amplitude at the third-harmonic frequency.

Describing the brain as a nonlinear elastic solid is theoretically complex due to high-order tensors in the strain-energy density [33,34]. By assuming a linear polarization, the general description can be reduced to a simpler scalar representation [35], while still retaining the nonlinearities that produce complex-wave physics [36,37]. For a plane polarized shear wave, the equation of motion for the particle velocity $v(x,t)$ can be written as

$$\frac{\partial v}{\partial x} - \frac{\beta}{c_t^3} v^2 \frac{\partial v}{\partial \tau} = \delta \frac{\partial^2 v}{\partial \tau^2}, \tag{1}$$

where $\tau = t - x/c_t$ is the retarded time with respect to the physical time t, x is the propagation distance, and β quantifies the nonlinearity. The term on the right-hand side accounts for dissipation, which has a significant influence on the shock dynamics. Equation (1) has a similar form to the well-known Burgers equation [38], except that the nonlinear term is cubic rather than quadratic. This equation is almost unstudied from the experimental point of view due to the difficulty of directly observing shear waves at depth in solids. As the wave propagates, the peaks and troughs are distorted by the cubic nonlinearity, which locally increases the shear wave speed as

a function of amplitude. Therefore, the wave will eventually "tip" over forming shocks for both the positive and negative wave phases. The cubic nonlinearity has a recognizable impact on the spectral development that occurs with propagation because it produces only odd harmonics.

The experimental development of this nonlinearity and its very specific odd-harmonic signature can be observed in the particle velocity [Fig. 2(b)] and the power spectrum [Fig. 2(c)]. This is direct evidence of shear-shock-wave development in the brain. The Rusanov scheme, along with the previously measured frequency-dependent attenuation, is used to fit the experimental data at $x = 6.5$ mm to Eq. (1). This numerical simulation allows us to estimate $\beta \approx 13 \pm 6$, producing excellent agreement between the theory (the black curve) and the experiment [36,39]. In the frequency domain, consistent with theoretical predictions, energy is transferred from the fundamental frequency to the odd harmonics. Furthermore, more energy is sent to the odd harmonics as the initial wave amplitude increases [Fig. 2(d)]. The third-harmonic amplitude as a function of the propagation distance [Fig. 2(d)] indicates that the peak nonlinearity occurs at a propagation distance of between 6 and 7 mm that is independent of initial velocity. Beyond this distance, viscosity overcomes nonlinear harmonic generation. The close match between the theoretical prediction and the observation indicates that nonlinearity is a first-order parameter required to accurately describe shearing mechanisms in the brain.

Note that, in contrast to Eq. (1), a significant but small portion of the fundamental energy is also transferred to even harmonics. This difference from theoretical predictions may be due to the brain structure, which is heterogeneous, and it therefore violates the assumption of homogeneity. In fact, it is surprising that the brain heterogeneity has so little influence on harmonic development. We believe that this is a consequence of the shear wavelength, 28.5 ± 0.8 mm at 75 Hz, which is larger than the characteristic structures in the porcine brain, such as vessels and sulci, and which therefore leads to weak wave–brain structure interactions.

The particle acceleration, which is more relevant to brain injury than particle velocity [2], is calculated with a broadband derivative in frequency [40]. Numerical differentiation is noise sensitive, especially at the sharp shock profiles [see Fig. 2(b)], and is due to false peak errors from of the tracking algorithm [24]. A number of validation steps are therefore performed to determine the error in the derivative calculations (see Appendix D). They are shown to be in good agreement with the numerical simulations.

The resulting particle acceleration has a large amplitude that is finely concentrated at the shock front as it propagates in the brain [Fig. 3(a) and Ref. [25]]. The shear wave grows, peaks, and dissipates within the first few centimeters of propagation. As a shear wave with an initial acceleration of 449 m/s^2 propagates in the brain, the steepening of the

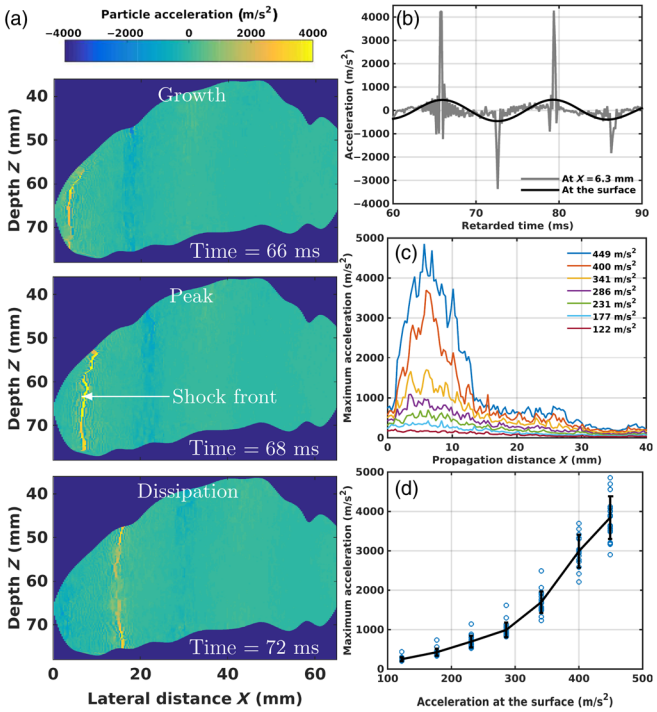

FIG. 3. (a) Snapshots of the particle acceleration showing the growth, peak, and dissipation of the shock front. (b) Time waveform of the acceleration signal at the surface of the brain and at 6.3 mm for an initial amplitude of 449 m/s^2. (c) The peak acceleration as a function of propagation distance. (d) Maximum peak acceleration as a function of acceleration at the surface of the brain. The circles represent the measurements of the four brains and the five independent imaging slices. The solid line is the average curve and the error bars show the standard deviation.

shock front amplifies the velocity gradient until it reaches 4200 m/s^2 at its peak, which is at $x = 6.3$ mm of propagation [Fig. 3(b)]. Thus, the acceleration in the brain is 9.3 times greater than the acceleration at the surface of the brain. The peak acceleration into the brain consistently occurs at $x = 6.3$ mm for the range of initial conditions considered here [Fig. 3(c)]. Furthermore, the maximum acceleration within the brain increases rapidly as the surface excitation increases, i.e., it is strongly nonlinear [Fig. 3(d)]. At the maximum surface excitation, the average amplification factor is 8.5.

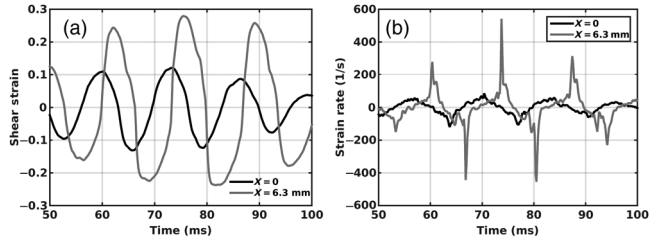

FIG. 4. (a) Strain and (b) strain rate at the surface (black curve) and at $x = 6.3$ mm (gray curve). The initial condition is 449 m/s^2.

In addition to acceleration, shear strain and strain rate are often used to predict brain injury [7,15]. Both are shown in Fig. 4. The shear strain has an amplitude of 0.12 and 0.28 at the surface and at 6.3 mm, i.e., an amplification factor of 2.3. The nonlinear distortion of the strain with propagation, which is similar to what is observed for the velocity, generates a dramatic increase in the strain rate at the shock front [see Figs. 4(b) and 2(b)]. The formation of the shock generates an amplification factor of 6.4 with respect to the brain surface. These shear-strain and strain-rate amplitudes are above the thresholds for an injury estimated for TBI (0.07 of strain and 40 s^{-1} for strain rate) [15].

In a real-life impact, the skull, the reflective fluid-solid interfaces, and the nonpolarized initial conditions generate more complex and disorganized shear waves than a plane wave. In this highly complex scenario, we believe that, at peak locations, a shock front will be locally generated, magnifying the local acceleration, shear strain, and strain rate experienced by neuronal tissue. This etiology is consistent with diffuse axonal injury, one of the most common and devastating forms of TBI, which consists of numerous small [(1–15)-mm] lesions that are distributed deep in the brain, far from the area of impact.

IV. CONCLUSION

By directly measuring brain motion with high-frame-rate ultrasound techniques, we demonstrate in this article that the combination of nonlinearity and attenuation is sufficient to develop shear shock waves over short propagation lengths starting from a smooth, low-impact shear wave in the *ex vivo* porcine brain. These shear shocks are formed in a frequency, a velocity amplitude, and an acceleration amplitude range that are within the envelope commonly observed in traumatic impacts. The physical mechanism from which this shear shock wave is generated is consistent with theoretical predictions of cubic nonlinearities that have a specific and readily identifiable odd-harmonic signature. The imaging techniques and shock-wave tracking methods developed here are not restricted to the brain, and they can be applied to soft tissue anywhere in the body that is accessible to conventional ultrasound imaging.

ACKNOWLEDGMENTS

The authors would like to acknowledge funding from the National Institutes of Health (Grant No. R01-NS091195). They would also like to thank Gregg Trahey and Francisco Melo for their comments on the manuscript.

APPENDIX A: MECHANICAL CHARACTERIZATION OF THE BRAIN

Nonlinear propagation transfers energy from a signal's fundamental frequency to higher frequencies via harmonic generation. To avoid the complex frequency-dependent interaction between nonlinearity, attenuation, and velocity,

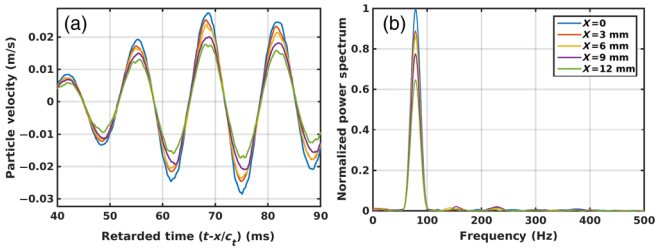

FIG. 5. (a) Particle velocity and (b) power spectrum generated by a linear shear wave traveling through the brain at different propagation distances.

measurements of the mechanical properties of the brain have to be performed in the linear regime. To characterize these linear mechanical parameters of the brain, a low-amplitude 2-m/s^2, 75-Hz excitation is used to generate a shear wave. The particle velocity for different propagation distances in the brain, $x = 0$, 3, 6, 9, and 12 mm (Fig. 5), shows that, as the shear wave propagates in the brain, there is a decrease in amplitude but no measurable harmonic generation. This observation confirms that subsequent measurements of attenuation and dispersion are performed in the linear regime and are independent of the effects of nonlinearity.

To measure the linear mechanical properties of the brain, the amplitude (A) and the phase (ϕ), as a function of the distance of propagation (x), are extracted from the Fourier transform of the experimentally measured particle velocity for the fundamental frequency. The attenuation, α, is obtained by fitting the expression $A(x) = e^{-\alpha x}$ to the measured amplitude. The average characteristic attenuation length is found to be $L_A = 1/\alpha = 25 \pm 2$ mm. The shear speed, c_t, is determined by fitting the experimentally measured phase to a linear phase shift, given by $\phi(x) = x\omega/c_t + \phi_0$, where ω is the angular frequency and ϕ_0 is an arbitrary reference phase. The average shear speed is found to be 2.14 ± 0.06 m/s. Here, the error represents the standard deviation across the four brain samples.

APPENDIX B: IMAGING SEQUENCES AND VALIDATION

To validate the proposed shock-tracking ultrasound imaging sequence, referred to as flash focus, two experiments are performed in the brain with a driving amplitude of 449 m/s^2. The first imaging sequence consists of a flash-focus sequence at one transducer position. The second sequence consists of the gold-standard conventional plane-wave compounding scheme [29], and each plane wave has a different angle of propagation in the x-z plane. To remain comparable to the flash-focus acquisition time, we use 15 angles and one transmit-receive event per angle. These angles are chosen to be equally spaced between $\pm 18°$ with respect to the z axis. Each angle is synchronized with the shear wave emission. After the multiple angles are

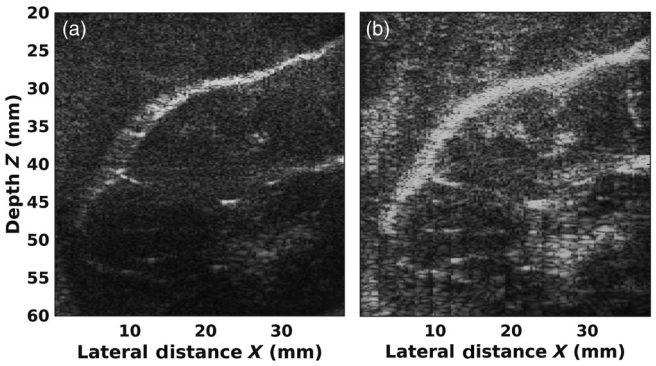

FIG. 6. Comparison of the B-mode images obtained from (a) a conventional plane-wave compounding and (b) a flash-focus sequence.

acquired, the data are beam formed to generate 1200 frames of rf data at 6200 frames/s.

Figure 6 shows the B-mode image corresponding to (a) a conventional plane-wave compounding and (b) a flash-focus sequence. The interframe displacement is calculated from the beam-formed rf data with the same adaptive tracking algorithm for both cases, and the resulting particle velocity is shown in Fig. 7(a) for plane-wave compounding, and in Fig. 7(b) for flash focus. It is qualitatively apparent from this figure that the flash-focus sequence provides a more uniform estimate of motion that is consistent with a planar shear wave. The time plot, shown in Fig. 8(a), is smoother for the flash-focus sequence, and, unlike the plane-wave compounding sequence, it does not exhibit the discontinuities that are characteristic of false-peak motion-tracking errors [41]. The frequency spectrum for the flash-focus sequence [Fig. 8(b)] is consistent with the theoretical predictions for odd-harmonic generation, whereas the plane-wave compounding angle exhibits a second-harmonic artifact which is much larger than any of the odd harmonics in its spectrum.

For a more quantitative comparison of the improvement generated by the flash-focus sequence, the average spectrum is computed for two regions, first in the surrounding

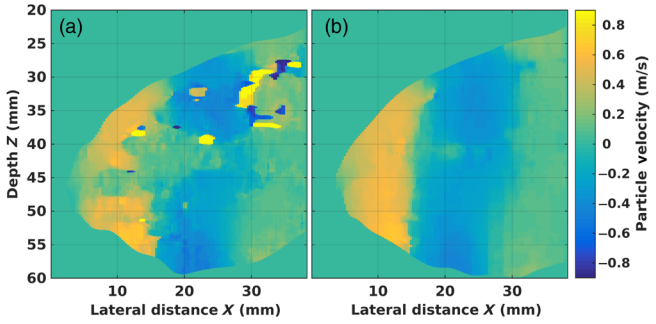

FIG. 7. Comparison of the particle-velocity measurement obtained from (a) a conventional plane-wave compounding and (b) a flash-focus sequence. Note that the color scale for both images is the same, and that a few regions in (a) are out of range.

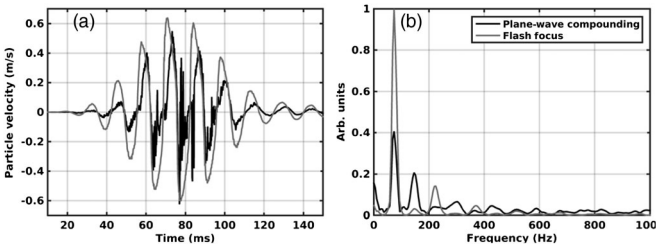

FIG. 8. (a) The time-domain waveform and (b) its corresponding frequency spectrum for the plane-wave compounding and flash-focus sequences at 45 mm of depth and at a propagation distance of $X = 10$ mm.

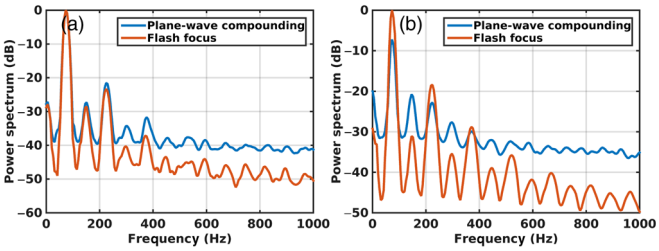

FIG. 9. Average power-spectrum measure in (a) the gelatin and (b) the brain with the plane-wave compounding and flash-focus sequences.

gelatin [Fig. 9(a)], then in the brain [Fig. 9(b)]. Figure 9(a) indicates that the two sequences generate results similar to the gelatin. The only significant improvement is a reduction of 14 dB of the noise floor when the flash-focus sequence is used. By contrast, in the brain region, plane-wave compounding underestimates the fundamental component by 7.2 dB, it overestimates the second harmonic by 10.3 dB, and it underestimates the third harmonic by 4.4 dB. Furthermore, the flash-focus sequences reduce the noise floor by 14.1 dB, allowing visualization up to the ninth harmonic. Therefore, the flash-focus sequence is a significant improvement that allows the observation and characterization of nonlinear shear waves propagated in the brain tissue.

APPENDIX C: VALIDATION OF THE TRACKING ALGORITHM

The shock front of a shear wave is sharp and consequently has wide support in the spectral domain. Detection of the motion produced by the shock front is challenging for tracking algorithms because the numerous high-frequency harmonics are at a significantly lower amplitude than the fundamental, but they define the shape and rise time of the shock front [24]. Our experimental setup does not afford opportunities for direct validation of the adaptive tracking algorithm since there is no *a priori* knowledge of brain motion. Therefore, the adaptive tracking algorithm is validated with two simulation tools, one for nonlinear shear propagation [36] and another for ultrasound imaging of particle displacements [32].

First, the particle displacement is determined by solving the nonlinear elastic wave equation [Eq. (1)] with a Rusanov scheme [36,39]. This method enables us to solve nonlinear hyperbolic equations with third-order accuracy and low computational time. The linear and nonlinear coefficients in this equation are assigned the values that are measured in the porcine brains, $c_t = 2.14$ m/s, $L_A = 25$ mm, and $\beta = 13 \pm 6$. The Chebyshev-enveloped 75-Hz signal that is used in the experiments is also used as an initial condition of the numerical solution. An initial amplitude of 0.8 m/s is chosen since it represents the high range of what is currently achievable by our experimental setup.

Then the output of this simulation is used to determine the position of the acoustical scatterers in a second simulation of ultrasound propagation. This second simulation tool consists of a finite-difference-time-domain solution of the full acoustic wave equation that we previously developed and used to model small particle displacements and to generate highly realistic ultrasound images [31,32]. Here, it is used to model the field generated by the ultrasound imaging system with the same transducer geometry and transmit-receive imaging sequence. The acoustical maps generated for the simulation have the gross acoustical properties of soft tissue, i.e., an average density of 1000 kg/m^3, a sound speed of 1540 m/s, and an attenuation coefficient of 0.3 dB/MHz cm. To obtain accurate speckle statistics, subwavelength scatterers with a size of 39 μm, a concentration > 20 scatters per resolution cell, and a random speed of sound between 1540 and 1502 m/s are distributed randomly in the medium. A separate acoustical map is generated for each of the 1200 frames and, in each map, the scatterers are displaced according to the time-dependent displacement previously generated by the numerical solution of Eq. (1).

The macroscopic view of two scatter maps, one displaced with respect to the other, is shown in Fig. 10(a). In the mesoscopic scale [Fig. 10(b)], the reference scatter map is shown in red and the displaced scatter map is shown in blue. Note that the displacement changes as a function of the lateral position. Subresolution displacement is represented by shifting the relative impedance of the two elements that represent a single scatter [Fig. 10(c)]. This is known as the impedance flow method [32].

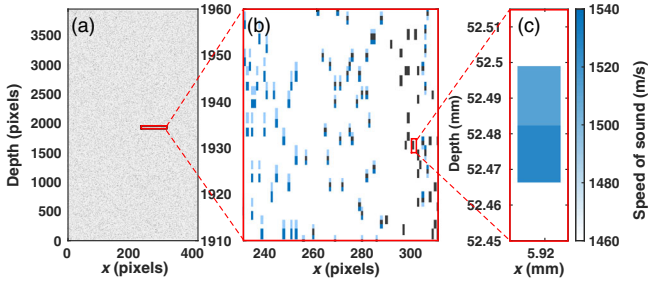

FIG. 10. A realization of the acoustic map used in the finite-difference-time-domain simulation of acoustic propagation and ultrasound imaging. The simulation domain consists of (a) subwavelength scatterers that are shifted by (b) a small amount determined by solution to Eq. (1) using (c) an impedance flow method to shift the scatterers by a subgrid displacement.

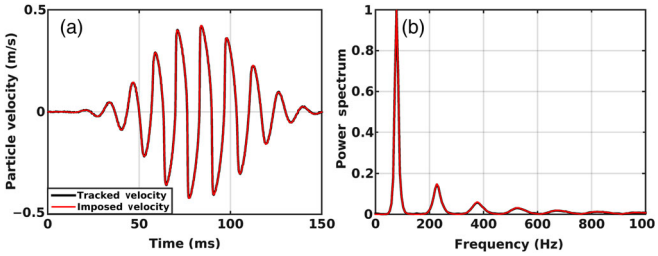

FIG. 11. Comparison between the imposed (red curve) and tracked (black curve) particle velocity in (a) the time domain and (b) the frequency domain. The tracked velocity is obtained from the simulated and beam-formed rf data, and the imposed velocity is obtained from a numerical solution of the one-dimensional nonlinear elastic wave equation [Eq. (1)]. Note that the curves appear to be superimposed.

In this scatter, the displacement is less than a pixel. For that reason, the displacement is imposed using the impedance flow method. A transmit-receive acoustical simulation is performed for each map to generate the raw rf data *in silico*. The simulated rf data are matched to experimental data by down sampling and then adding white noise to achieve the 20-dB SNR observed in the *ex vivo* brain experiment. Then the rf data are beam formed using the same aperture and delay-and-sum methods that were previously used experimentally. Thus, 1200 frames are finally processed with the adaptive tracking code to estimate particle motion [24].

The imposed shear wave calculated from Eq. (1) is shown as a red curve in the left panel of Fig. 11. It is almost indistinguishable from the ultrasound-based motion estimate shown as a black curve (the two are superimposed), and the root-mean-square difference between these two curves is 2.1%. The corresponding power spectrum [Fig. 11(b)] is also superimposed, which confirms that the ultrasound imaging sequence and the adaptive tracking algorithm preserve the spectral content of the particle motion and can accurately capture the higher harmonics that are necessary for the characterization of the shock front.

The final validation step for the tracking algorithm and its ability to represent the harmonics is performed with experiments driven at a low amplitude that is assumed to be linear (0.03 m/s). In this experiment, shown in Fig. 5, the second and third harmonics represent less that 2.0% of the amplitude of the fundamental component. Thus, the waveform does not distort nonlinearly with propagation. This experiment not only confirms the initial assumption of linearity but also eliminates the possibility that the nonlinear behavior observed experimentally is a tracking-algorithm-based artifact.

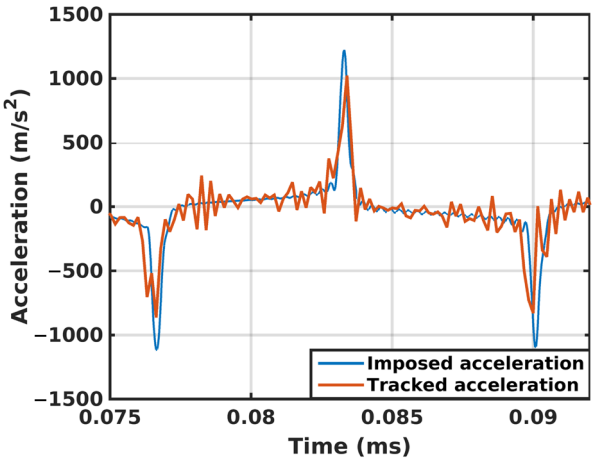

FIG. 12. Comparison between the imposed and the tracked acceleration calculated with a Fourier-based method.

APPENDIX D: DIFFERENTIATION METHOD

Numerical differentiation, on which our estimates of acceleration from velocity rely, can be noise sensitive, especially since the derivatives must be accurate at the steep shock front. The acceleration $a(t)$ is computed from the experimental data with a standard derivative in the Fourier domain [40].

To determine the expected error in acceleration, the derivative of the known velocity determined by the simulation of Eq. (1) is compared to the derivative of the ultrasound-based velocity. Since the imposed velocity is calculated numerically, it does not include experimental noise and it is sampled at high frequency (10 times the experimental sampling). Thus, its time derivative is robust and does not depend on the method used for differentiation. On the other hand, the experimental velocity is obtained by applying our tracking algorithm to the simulated rf data as described in the previous section. Therefore, the simulated tracked velocity has similar noise characteristics and the same sampling frequency (6200 Hz) as the experimental data, where the actual velocity is unknown *a priori*. These acceleration calculations (Fig. 12) show that, even though this method increases high-frequency noise proportionally to ω, it preserves the acceleration peaks at the shock front and underestimates them by approximately 15%. This result indicates that estimates of the shock-front magnification factors reported in the main text are conservatively low.

[1] R. W. Rimel, B. Giordani, J. T. Barth, T. J. Boll, and J. A. Jane, Disability caused by minor head injury, Neurosurgery Q. **9**, 221 (1981).

[2] S. Rowson and S. M. Duma, Brain injury prediction: Assessing the combined probability of concussion using linear and rotational head acceleration, Ann. Biomed. Eng. **41**, 873 (2013).

[3] S. P. Broglio, J. J. Sosnoff, S. Shin, X. He, C. Alcaraz, and J. Zimmerman, Head impacts during high school football: A biomechanical assessment, J. Athletic Training **44**, 342 (2009).

[4] J. J. Crisco, B. J. Wilcox, J. G. Beckwith, J. J. Chu, A.-C. Duhaime, S. Rowson, S. M. Duma, A. C. Maerlender, T. W. McAllister, and R. M. Greenwald, Head impact exposure in collegiate football players, J. Biomech. **44**, 2673 (2011).

[5] R. W. Daniel, S. Rowson, and S. M. Duma, Head impact exposure in youth football, Ann. Biomed. Eng. **40**, 976 (2012).

[6] K. Laksari, L. C. Wu, M. Kurt, C. Kuo, and D. C. Camarillo, Resonance of human brain under head acceleration, J. R. Soc. Interface **12**, 20150331 (2015).

[7] R. M. Wright and K. T. Ramesh, An axonal strain injury criterion for traumatic brain injury, Biomech. Model. Mechanobiol. **11**, 245 (2012).

[8] K. M. Guskiewicz, J. P. Mihalik, V. Shankar, S. W. Marshall, D. H. Crowell, S. M. Oliaro, M. F. Ciocca, and D. N. Hooker, Measurement of head impacts in collegiate football players: Relationship between head impact biomechanics and acute clinical outcome after concussion, Neurosurg. Q. **61**, 1244 (2007).

[9] P. Bayly, T. Cohen, E. Leister, D. Ajo, E. Leuthardt, and G. Genin, Deformation of the human brain induced by mild acceleration, J. Neurotrauma **22**, 845 (2005).

[10] W. C. Moss, M. J. King, and E. G. Blackman, Skull Flexure from Blast Waves: A Mechanism for Brain Injury with Implications for Helmet Design, Phys. Rev. Lett. **103**, 108702 (2009).

[11] A. Goriely, J. Weickenmeier, and E. Kuhl, Stress Singularities in Swelling Soft Solids, Phys. Rev. Lett. **117**, 138001 (2016).

[12] K. Darvish and J. Crandall, Nonlinear viscoelastic effects in oscillatory shear deformation of brain tissue, Med. Eng. Phys. **23**, 633 (2001).

[13] B. R. Donnelly, Shear properties of human brain tissue, J. Biomech. Eng. **119**, 423 (1997).

[14] S. S. Margulies and L. E. Thibault, A proposed tolerance criterion for diffuse axonal injury in man, J. Biomech. **25**, 917 (1992).

[15] S. Sullivan, S. A. Eucker, D. Gabrieli, C. Bradfield, B. Coats, M. R. Maltese, J. Lee, C. Smith, and S. S. Margulies, White matter tract-oriented deformation predicts traumatic axonal brain injury and reveals rotational direction-specific vulnerabilities, Biomech. Model. Mechanobiol. **14**, 877 (2015).

[16] U. Hamhaber, D. Klatt, S. Papazoglou, M. Hollmann, J. Stadler, I. Sack, J. Bernarding, and J. Braun, *In vivo* magnetic resonance elastography of human brain at 7 t and 1.5 t, J. Magn. Reson. Imaging **32**, 577 (2010).

[17] C. L. Johnson, M. D. McGarry, E. E. Houten, J. B. Weaver, K. D. Paulsen, B. P. Sutton, and J. G. Georgiadis, Magnetic resonance elastography of the brain using multishot spiral readouts with self-navigated motion correction, Magn. Reson. Med. **70**, 404 (2013).

[18] M. Razani, A. Mariampillai, C. Sun, T. W. Luk, V. X. Yang, and M. C. Kolios, Feasibility of optical coherence elastography measurements of shear wave propagation in

homogeneous tissue equivalent phantoms, Biomed. Opt. Express **3**, 972 (2012).
[19] S. Song, Z. Huang, and R. K. Wang, Tracking mechanical wave propagation within tissue using phase-sensitive optical coherence tomography: Motion artifact and its compensation, J. Biomed. Opt. **18**, 121505 (2013).
[20] M. Razani, T. W. Luk, A. Mariampillai, P. Siegler, T.-R. Kiehl, M. C. Kolios, and V. X. Yang, Optical coherence tomography detection of shear wave propagation in inhomogeneous tissue equivalent phantoms and *ex vivo* carotid artery samples, Biomed. Opt. Express **5**, 895 (2014).
[21] J.-H. Park, W. Sun, and M. Cui, High-resolution *in vivo* imaging of mouse brain through the intact skull, Proc. Natl. Acad. Sci. U.S.A. **112**, 9236 (2015).
[22] S. Catheline, J.-L. Gennisson, M. Tanter, and M. Fink, Observation of Shock Transverse Waves in Elastic Media, Phys. Rev. Lett. **91**, 164301 (2003).
[23] M. Tanter, J. Bercoff, L. Sandrin, and M. Fink, Ultrafast compound imaging for 2D motion vector estimation: Application to transient elastography, IEEE Trans. Ultrason. Ferroelectr. Freq. Control **49**, 1363 (2002).
[24] G. Pinton, J.-L. Gennisson, M. Tanter, and F. Coulouvrat, Adaptive motion estimation of shear shock waves in soft solids and tissue with ultrasound, IEEE Trans. Ultrason. Ferroelectr. Freq. Control **61**, 1489 (2014).
[25] See Supplemental Material at http://link.aps.org/supplemental/10.1103/PhysRevApplied.8.044024 for (a) a movie of the ultrasound *B*-mode images, (b) a movie of the particle velocity, and (c) a movie of the particle acceleration of the brain.
[26] F. Duck, *Physical Properties of Tissue: A Comprehensive Reference Book* (Academic Press, London, 1990).
[27] B. Giammarinaro, F. Coulouvrat, and G. Pinton, Numerical simulation of focused shock shear waves in soft solids and a two-dimensional nonlinear homogeneous model of the brain, J. Biomech. Eng. **138**, 041003 (2016).
[28] R. M. Greenwald, J. T. Gwin, J. J. Chu, and J. J. Crisco, Head impact severity measures for evaluating mild traumatic brain injury risk exposure, Neurosurg. Q. **62**, 789 (2008).
[29] G. Montaldo, M. Tanter, J. Bercoff, N. Benech, and M. Fink, Coherent plane-wave compounding for very high frame rate ultrasonography and transient elastography, IEEE Trans. Ultrason. Ferroelectr. Freq. Control **56**, 489 (2009).
[30] G. F. Pinton, G. E. Trahey, and J. J. Dahl, Sources of image degradation in fundamental and harmonic ultrasound imaging using nonlinear, full-wave simulations, IEEE Trans. Ultrason. Ferroelectr. Freq. Control **58**, 754 (2011).
[31] G. Pinton, Three dimensional full-wave nonlinear acoustic simulations of ultrasound imaging and therapy in the entire human body, in *Proceedings of the 2012 IEEE International Ultrasonics Symposium, Dresden, Germany, 2012* (IEEE, New York, 2012), pp. 142–145.
[32] G. Pinton, Subresolution displacements in finite difference simulations of ultrasound propagation and imaging, IEEE Trans. Ultrason. Ferroelectr. Freq. Control **64**, 537 (2017).
[33] L. D. Landau and E. M. Lifshitz, *Theory of Elasticity*, Course of Theoretical Physics Vol. 7 (Pergamon Press, New York, 1959).
[34] M. Wochner, M. Hamilton, Y. Ilinksii, and E. Zabolotskaya, Cubic nonlinearity in shear wave beams with different polarizations, J. Acoust. Soc. Am. **123**, 2488 (2008).
[35] E. Zabolotskaya, M. Hamilton, Y. Ilinskii, and G. Meegan, Modeling of nonlinear shear waves in soft solids, J. Acoust. Soc. Am. **116**, 2807 (2004).
[36] G. Pinton, F. Coulouvrat, J. Gennisson, and M. Tanter, Nonlinear reflection of shock shear waves in soft elastic media, J. Acoust. Soc. Am. **127**, 683 (2010).
[37] G. B. Whitham, *Linear and Nonlinear Waves*, Pure and Applied Mathematics (Wiley InterScience, New York, 1974).
[38] J. M. Burgers, A mathematical model illustrating the theory of turbulence, Adv. Appl. Mech. **1**, 171 (1948).
[39] V. Rusanov, On difference schemes of third order accuracy for nonlinear hyperbolic systems, J. Comput. Phys. **5**, 507 (1970).
[40] A. V. Oppenheim, A. S. Willsky, and S. H. Nawab, *Signals and Systems*, Vol. 2 (Prentice-Hall, Englewood Cliffs, NJ, 1983).
[41] G. F. Pinton, J. J. Dahl, and G. E. Trahey, Rapid tracking of small displacements with ultrasound, IEEE Trans. Ultrason. Ferroelectr. Freq. Control **53**, 1103 (2006).